Optical investigation of the thermoelectric topological crystalline insulator Pb$_{0.77}$Sn$_{0.23}$Se

Anjan A. Reijnders,[1,*] Jason Hamilton,[1] Vivian Britto,[1] Jean-Blaise Brubach,[2]
Pascale Roy,[2] Quinn D. Gibson,[3] R. J. Cava,[3] and K. S. Burch[4,†]

[1]*Department of Physics & Institute for Optical Sciences, University of Toronto, 60 St. George Street, Toronto, Ontario M5S 1A7, Canada*
[2]*Synchrotron SOLEIL, L'Orme des Merisiers Saint-Aubin, 91192 Gif-sur-Yvette, France*
[3]*Department of Chemistry, Princeton University, Princeton, New Jersey 08544, USA*
[4]*Department of Physics, Boston College, 140 Commonwealth Ave, Chestnut Hill, Massachusetts 02467, USA*

Pb$_{0.77}$Sn$_{0.23}$Se is a promising thermoelectric alloy that exhibits a temperature dependent band inversion below 300 K. Recent work has shown that this band inversion also coincides with a trivial to nontrivial topological phase transition. To understand how the properties critical to thermoelectric efficiency are affected by the band inversion, we measured the broadband optical response of Pb$_{0.77}$Sn$_{0.23}$Se as a function of temperature. We find clear optical signatures suggesting the band inversion occurs at 160 ± 15 K, and use the extended Drude model to accurately determine a $T^{3/2}$ dependence of the bulk carrier lifetime, associated with electron-acoustic phonon scattering. Due to the high bulk carrier doping level, no discriminating signatures of the topological surface states are found, although their presence cannot be excluded from our data.

I. INTRODUCTION

Thermoelectrics are a subject of great interest to industry for their many applications as macro- and micro-scale Peltier coolers, their waste-heat energy recycling potential (heat-to-electricity conversion) in industrial and consumer products, and their application as highly sensitive compact and robust sensors [1–5]. An academic interest has also persisted as the optimization of thermoelectric efficiency offers an intriguing challenge in which ostensibly mutually exclusive physical properties must be combined in one material for the greatest performance. This is illustrated by the figure of merit $ZT = \frac{TS^2\sigma}{\kappa}$, where S, σ, and κ are the Seebeck coefficient, the DC conductivity, and the thermal conductivity, respectively. For high thermoelectric efficiency, S and σ must therefore be simultaneously enhanced, while κ is deliberately suppressed. This is a nontrivial task, considering the intimate link between the parameters that define ZT. For example, both σ and κ depend on the carrier lifetime τ, while both S and σ are a function of the band dispersion. Hence, the improvement of each individual quantity could result in an overall decrease of ZT, thus making experimental techniques that can disentangle the common limitations of each quantity highly desirable.

Currently, the primary methods of studying thermoelectrics are by DC transport, optics, thermopower experiments, and neutron scattering [6–15], where the standard Drude model is often employed to extract temperature dependent information about carrier lifetimes. A major shortcoming of the Drude model, however, is the assumption that the carrier lifetime is frequency independent. When analyzing optical data, this often results in poor quality Drude fits, and carrier scattering rates with large uncertainties. A solution to this shortcoming is the application of the *extended* Drude analysis to a sample's optical response [16]. While commonplace in the optical investigation of strongly correlated systems [17–21], the extended Drude model offers some benefits previously unexplored in the context of thermoelectrics. Using this approach grants access not only to the temperature dependence of the carrier lifetime, but also to its frequency dependence, shedding light on the various scattering mechanisms that govern σ and κ. Moreover, with both high temperature and energy resolution [22], broadband (far infrared through visible) optical spectroscopy provides direct access to the free carrier plasma frequency and band mass, both affecting S and σ, as well as spectral weight transfers and band transitions, useful for studying band gaps and band inversions.

To illustrate the versatility of this approach, we have performed our measurements on Pb$_{0.77}$Sn$_{0.23}$Se, a compound comprising thoroughly studied binary constituents PbSe and SnSe [9–12,23–28]. However, unlike its constituents, previous works on Pb$_{0.77}$Sn$_{0.23}$Se crystals have shown evidence of a temperature dependent band inversion, although neither the exact transition temperature nor the temperature dependence of the gap has been identified conclusively. This is largely a result of limited energy and temperature resolution of the experimental probes that were used, with various reports ranging between 80 and 200 K [6,8,9,25,29–31]. Hence, broadband optical spectroscopy provides a unique opportunity to study, in a very controlled manner, how carrier dynamics change throughout the inversion. Moreover, many traditional thermoelectric probes, such as transport and Seebeck measurements, rely on band structure models to extract the scattering rate. Such band structure assumptions are severely complicated by the band inversion, further motivating the investigation of Pb$_{0.77}$Sn$_{0.23}$Se by optical spectroscopy, as features of the band inversion and the carrier lifetime can be measured independently in a single experiment. This discriminating quality becomes even more evident by considering previous transport studies of the Pb$_{1-x}$Sn$_x$Se system. While Pb$_{1-x}$Sn$_x$Se alloys have been studied for 50 years [32], only specially prepared low-carrier extrinsic p-type Pb$_{0.77}$Sn$_{0.23}$Se was found to show abrupt changes in the DC transport properties across the band inversion [8]. Interestingly, as-grown n-type crystals showed

_____

*Present address: Montana Instruments, 151 Evergreen Drive, Bozeman, Montana 59715, USA; reijnder@physics.utoronto.ca
†burchke@bc.edu

no clear signatures of the band inversion at all. A recent paper by Liang *et al.* highlighted this peculiarity and was the first to show evidence of the band inversion in *n*-type $Pb_{0.77}Sn_{0.23}Se$, employing Nernst and thermopower experiments [6]. Particularly for device applications, a thorough understanding of the electronic properties of both *n*- and *p*-type crystals is pivotal [26].

The temperature dependent band inversion of $Pb_{0.77}Sn_{0.23}Se$ has also received significant attention from the topological insulator community. It was recently shown that while PbSe is a trivial insulator, the $Pb_{1-x}Sn_xSe$ system becomes a topological crystalline insulator (TCI) above a critical *x* value; a state of matter in which crystal point group symmetry protects the persistence of gapless surface states with a spin polarized Dirac dispersion [27,29,31,33,34]. Interestingly, in $Pb_{0.77}Sn_{0.23}Se$ we have the unique opportunity to tune between topological and trivial phases using temperature rather than doping, thus negating the effects of disorder. Moreover, since it is challenging to perform angle-resolved photoemission spectroscopy (ARPES) and scanning tunneling microscopy (STM)—the primary methods of studying surface states—at various temperatures, temperature dependent broadband spectroscopy makes a great tool for the investigation of surface states in topological (crystalline) insulators [26,27,31,35–43]. We note that since band gaps are typically tuned by electron-phonon coupling and anharmonicity, the concurrent band inversion and topological phase transition hints at a more subtle process. Hence, $Pb_{0.77}Sn_{0.23}Se$ can reveal new insights into how anharmonicity, electron-phonon coupling, and topology all interplay.

In the present work, we measure the temperature dependent broadband reflectance of $Pb_{0.77}Sn_{0.23}Se$ between 5 and 292 K, and extract its optical conductivity and dielectric function between 6 meV and 6 eV. Subsequent extended Drude analysis reveals the frequency dependent free carrier scattering rate, and is used for a precise determination of the dominant temperature dependent scattering mechanism. We find clear optical signatures sugestive of a band inversion temperature at 160 ± 15 K by studying the free carrier plasma frequency and direct optical band gap transitions. Interestingly, the temperature dependent free carrier scattering rate shows no signatures of the band inversion, and follows $T^{3/2}$ behavior in accordance with electron-acoustic phonon scattering. Finally, we find that the Fermi level lies deep in the conduction band (114 ± 22 meV), obscuring the observation of surface states [35,44–46], and causing the Seebeck coefficient and power factor to be insensitive to the band inversion.

II. EXPERIMENT

$Pb_{0.77}Sn_{0.23}Se$ crystals were grown at Princeton University by sealing the elements in evacuated quartz ampoules in stochiometric ratios. The samples were then heated to $1000\,^{\circ}C$ for two weeks, followed by quenching in air to room temperature. The samples were then annealed at $400\,^{\circ}C$ for one week. Purity and stoichiometry were assessed by x-ray diffraction. Prior to the reflectance measurements, samples were freshly cleaved with a razor blade to produce a lustrous surface.
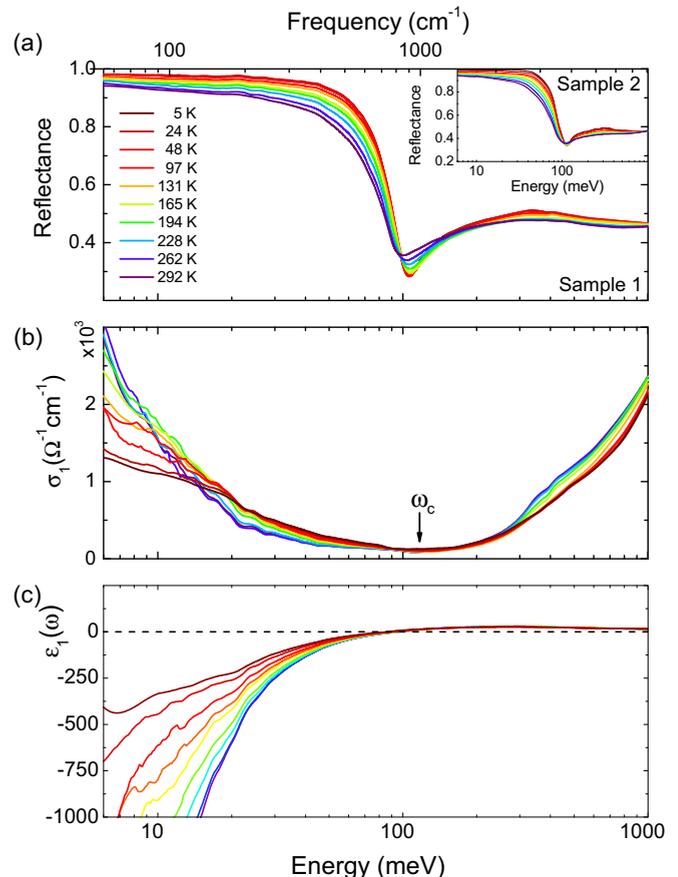
FIG. 1. (Color online) (a) The changing slope in the reflectance below the plasma edge (reflectance minimum) indicates a temperature dependent free carrier scattering rate in $Pb_{0.77}Sn_{0.23}Se$. (b) The optical conductivity reveals a clear separation (ω_c) between Drude conductivity below 125 meV, and inter/intra-band transitions above 125 meV. (c) The zero-crossing of the real part of the dielectric function (ϵ_1), indicative of the screened plasma frequency, can be used to determine ϵ_∞.

Cleaving by tape was also attempted, but proved unsuccessful in producing high quality surfaces. Temperature dependent reflectance measurements were performed in near-normal geometry between 6 meV and 1.5 eV, using a modified Bruker VERTEX 80v and ARS continuous flow cryostat, described in detail elsewhere [35] [Fig. 1(a)]. Reflectance data below 12 meV were corroborated by repeating the measurements using synchrotron radiation and a custom designed sample chamber with a closed cycle Cryomech cryostat at the AILES Beamline of the SOLEIL synchrotron in France. All infrared data were complemented by partially overlapping room temperature ellipsometry measurements between 0.75 and 6 eV.

Using RefFIT, a simultaneous variational dielectric fit (VDF) of reflectance and ellipsometry data yielded all Kramers-Kronig consistent optical constants. All measurements were performed on two different crystals from the same sample batch, showing excellent qualitative resemblance [see inset of Fig. 1(a) for the reflectance of sample 2]. Hence, data from only one crystal are discussed.

III. RESULTS AND ANALYSIS

Figure 1(b) shows the real part of the optical conductivity $\sigma_1(\omega)$ of $Pb_{0.77}Sn_{0.23}Se$ in the far and mid infrared. The spectra are dominated by a distinct Drude peak below 125 meV, associated with free carrier conductivity, and separated by a cutoff frequency ω_c from the interband transitions above 125 meV.

The simplest approach to understanding the spectral range below ω_c is to apply the semiclassical Drude model, in which the complex dielectric function for the free carrier response is given by

$$\hat{\epsilon}(\omega) = \epsilon_\infty - \frac{\omega_p^2}{\omega^2 + i\frac{\omega}{\tau}}, \tag{1}$$

where ω_p is the bare plasma frequency, τ is the transport lifetime, and ϵ_∞ captures all contributions to the dielectric function other than the Drude conductivity (i.e., interband transitions and polarizability of the static background). The bare plasma frequency is defined as $\omega_p^2 = 4\pi n e^2/m_b$, where n is the carrier density and m_b is the band mass.

An immediate consequence of this model is the large, low frequency negative contribution to the real part of the dielectric function ($\hat{\epsilon} = \epsilon_1 + i\epsilon_2$) due to the free carrier response. Indeed from Eq. (1) it can be seen that in the limit $\omega\tau \gg 1$ the zero-crossing of ϵ_1 corresponds to the screened plasma frequency $\tilde{\omega}_p$, which is related to the bare plasma frequency ω_p through $\omega_p = \tilde{\omega}_p\sqrt{\epsilon_\infty}$. Hence, we expect to observe this zero-crossing in ϵ_1, which can be seen directly in Fig. 1(c). The temperature dependence of both ω_p and ϵ_∞ are discussed next.

Before analyzing the spectra in detail, it is useful to consider what we expect to observe as a result of the band inversion. For compounds in which the chemical potential is located in the bulk gap, a distinct signature of a band inversion would be the spectral weight redistribution from interband transitions to the Drude conductivity. As the gap closes, the onset frequency of the interband transitions [roughly ω_c in Fig. 1(c)] moves to lower energy, until it merges with the Drude when the gap size reduces to zero. However, since as-grown $Pb_{0.77}Sn_{0.23}Se$ is naturally n type [chemical potential in the conduction band, shown in Fig. 2(a)], we do not expect to observe such obvious behavior, and therefore perform more sophisticated analysis to observe the band inversion. Figure 2(b) illustrates how the band inversion could be deduced from signatures in $\sigma_1(\omega)$. Region I is dominated by free carrier behavior, described by Eq. (1). Hence, as the band dispersion transforms across the band inversion [Fig. 2(a)], changes in both m_b and n can result in an unusual temperature dependence of the plasma frequency [where $\omega_p^2 \propto$ spectral weight in $\sigma_1(\omega)$]. One might also expect the inversion driven changes in the electronic structure to be reflected in the carrier lifetime. This can be seen from the width of the Lorentzian features (centered at 0), while deviations from the Lorentzian lineshape indicate an energy dependent lifetime. Region III can be used to extract the magnitude of the direct gap transitions E_{dir} shown in Fig. 2(a). With the chemical potential (μ) in the conduction band, the smallest allowed E_{dir} is offset from the conduction band minimum. Hence, changes in the band dispersion as well as n are likely to affect E_{dir}, resulting in a shift of the interband transition onset in $\sigma_1(\omega)$, as shown in Fig. 2(b). Since ϵ_∞ is a measure of the spectral
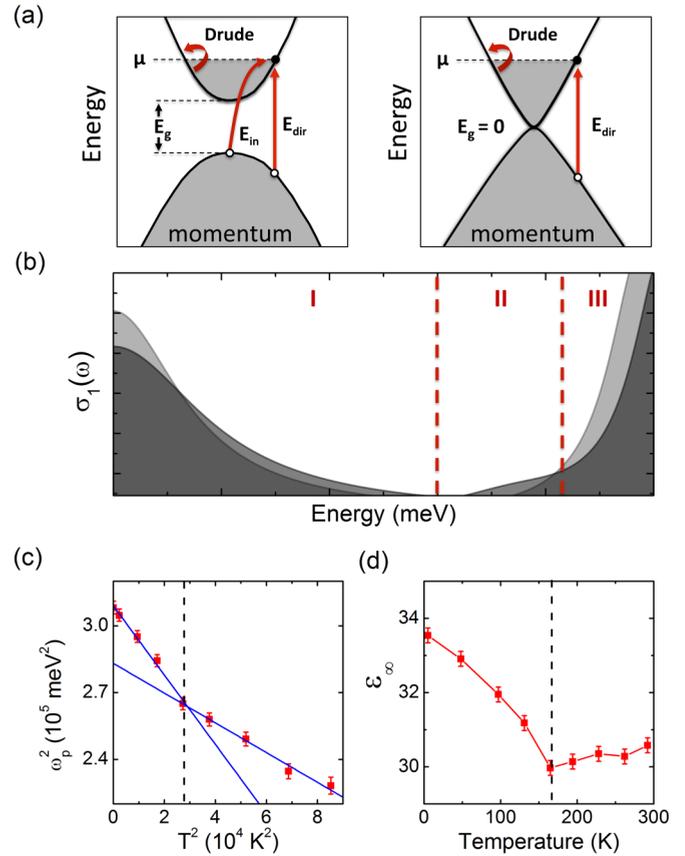
FIG. 2. (Color online) (a) Band structure diagram before or after the band inversion (left panel), and during the inversion (right panel), illustrating the allowed (in)direct transitions when the chemical potential is in the bulk conduction band (as is the case in as-grown $Pb_{0.77}Sn_{0.23}Se$). (b) Signatures of this inversion include a changing free carrier lifetime $\tau(T,\omega)$ and plasma frequency ω_p (region I), spectral weight change for indirect gap transitions (region II), and changes in the size of the direct gap (region III). (c) The plasma frequency of $Pb_{0.77}Sn_{0.23}Se$ shows a distinct change in temperature dependence around 160 K, deviating from its expected quadratic temperature dependence. (d) ϵ_∞ also shows an abrupt change in its temperature dependence at 160 K, further suggesting 160 K as the band inversion temperature.

weight in σ_1 above the free carriers, this quantity too should reveal signatures of the band inversion, similar to E_{dir}. Finally, below E_{dir}, region II is sensitive to temperature dependent changes in indirect gap transitions E_{in}, where $E_{in} < E_{dir}$, as well as impurity scattering responsible for an extended E_{dir} onset (known as an Urbach tail [47]).

A. Bulk plasma frequency and ϵ_∞

The spectral weight of the Drude feature (area under σ_1) is a direct measure of the bare plasma frequency squared, ω_p^2, and was determined by integrating $\sigma_1(\omega)$ up to a cutoff point ω_c using

$$\omega_p^2 \simeq \frac{120}{\pi}\int_0^{\omega_c}\sigma_1(\omega')\,d\omega', \tag{2}$$

where ω_c separates the Drude contribution to $\sigma_1(\omega)$ from the interband transitions [as indicated in Fig. 1(b)] [21]. The bare plasma frequency was then used to extract $\epsilon_\infty(T)$ from the zero-crossing in $\epsilon_1(\omega)$. We note that the values for $\epsilon_\infty(T)$ were corroborated by an alternative analytical method [21]. Here, the Drude contribution to the optical conductivity was manually removed from the data, followed by fitting the optical conductivity data to obtain the complex dielectric function. The value of $\epsilon_1(\omega = 0)$ is then a measure of ϵ_∞, which in our analysis differed from our primary determination of ϵ_∞ only by a constant offset of a few percent.

The temperature dependence of ω_p^2 and ϵ_∞ are shown in Figs. 2(c) and 2(d), respectively. Starting with ω_p^2, we find a reduction as temperature increases, with a distinct discontinuity in the trend around 160 K. In general, a temperature dependent reduction in ω_p^2 is an expected result that can be understood as follows. While semiclassically we have $\omega_p^2 \propto n/m$, quantum mechanically the squared plasma frequency calculated using Eq. (2) corresponds to an integration of the density of states $[N(\omega,T)]$ multiplied by the Fermi function $[f(\omega,T)]$, so that $\omega_p^2(T) \propto \int N(\omega,T) f(\omega,T) \, d\omega$ [48,49]. Evaluating this integral using the Sommerfeld expansion yields a temperature independent term equal to ω_p^2 at 0 K, and a negative T^2 term as a result of thermal smearing of the Fermi function. Hence, the temperature dependence of the squared plasma frequency is expected to follow

$$\omega_p^2(T) \approx \omega_p^2(T = 0K) - BT^2, \qquad (3)$$

where B depends on $N(\omega,T)$ at the Fermi energy [48–50]. Interestingly, while a linear decline in ω_p^2 vs T^2 is expected, Fig. 2(c) shows two distinct regimes in its temperature dependence below and above 160 ± 15 K. Since B is a function of the density of states, this is a clear signature of an abrupt change in the band dispersion, associated with the band inversion. Indeed, this critical temperature falls within the 80–200 K temperature range over which the band inversion was previously observed [6,8,9,29,30,51]. This also provides a first indication that despite the Fermi level of n-type $Pb_{0.77}Sn_{0.23}Se$ not being in the gap, discontinuities in its optical properties are a useful probe in the investigation of its band inversion temperature.

Besides clear signatures of the band inversion in ω_p^2, we also expect to see a change in ϵ_∞ at 160 ± 15 K. Since ϵ_∞ is a measure of the spectral weight of all interband transitions, it is sensitive to temperature dependent changes in the band structure [52]. This is confirmed by Fig. 2(d), revealing a clear change in the temperature dependence around 160 K, and will be discussed in greater detail in Sec. III C.

B. Surface states

Besides the Seebeck sensitivity to the band inversion at 160 ± 15 K, this critical temperature is also relevant to the topological phase of $Pb_{0.77}Sn_{0.23}Se$. Previous studies have shown how the band inversion is accompanied by a topological phase transition, where at low temperature topologically protected surface states persist in the bulk band gap [6,29,30,33,51,53]. In our optical data below 160 K [Fig. 1(a)] we see no evidence of Dirac surface states, such as previously observed in topological insulators Bi_2Te_2Se,

Bi_2Se_3, and $(Bi,Sb)_2Te_3$ [35–40] This is not surprising since we find a bulk chemical potential of 114 ± 22 meV above the conduction band minimum at 5 K (shown later), consistent with previous studies of $Pb_{1-x}Sn_xSe$ with similar stoichiometry [6,29,30,51] Such a high bulk μ causes bulk conductance to dominate the optical properties, which can by understood by considering how the measured reflectance relates to the complex dielectric function, as $R = |(1 - \sqrt{\hat{\epsilon}})/(1 + \sqrt{\hat{\epsilon}})|^2$. From Fig. 1(c) and Eq. (1) it is clear that $|1 \pm \sqrt{\hat{\epsilon}}| \gg 1$ for all frequencies $\omega < \tilde{\omega}_p$, resulting in $R > 95\%$ over the full far infrared (FIR) range for most temperatures. Such high FIR reflectance even above the topological phase transitions obscures discriminating surface conductance signatures from the bulk conductivity in $R(\omega)$. Moreover, with the Fermi level so high in the conduction band, mixing of the surface and bulk bands also blurs other distinguishing features such as the bulk vs surface carrier lifetime. However, to ensure we did not overlook surface state signatures in our reflectance data, we used the Boltzmann transport equation to estimate their expected effect on the measured reflectance. Indeed, the surface state signatures are far below our detection sensitivity, as described in the Appendix, and crystals with a lower bulk carrier concentration are required for further optical investigations of the topological crystalline surface state properties of $Pb_{0.77}Sn_{0.23}Se$.

C. Interband transitions

To study how the bulk electronic structure is affected by the band inversion, we turn to the band gap transitions that are visible above ω_c in Fig. 1(b). With ARPES measurements showing μ high in the conduction band for crystals with identical stoichiometry [25,27,29,30,51], the smallest allowed direct gap transition exceeds the direct band gap, as illustrated in Fig. 2(a). This effect is known as the Burstein-Moss shift [11,54]. Assuming a parabolic dispersion for both the conduction and valence band, the energy of this transition can be estimated. By adding $\mu = \hbar^2 k_F^2 / 2m_c$ to the direct band gap energy E_g, and to the energy of the valence band electrons with respect to valence band maximum of $E_v = \hbar^2 k_F^2 / 2m_v$, the total transition energy at zero energy is given by

$$E_{dir} \approx E_g + \mu \left(1 + \frac{m_c}{m_v}\right). \qquad (4)$$

The magnitude of E_{dir} can be obtained from a linear fit of the squared absorption coefficient, where $\alpha^2 = C(\omega - E_{dir})$, as shown in Fig. 3(a) [54]. The temperature dependence of E_{dir} is shown in Fig. 3(b), revealing a rise at low temperature, and a peak value of $E_{dir} = 315 \pm 10$ meV around 160 K. This rise in energy is expected from $\mathbf{k} \cdot \mathbf{p}$ theory as the Fermi level for compounds with similar carrier density (1×10^{19} cm^{-3}) is predicted to rise and peak as $E_g \to 0$ [28]. A previous study of the doping dependent band inversion in the $Pb_{1-x}Sn_xTe$ system also found a change in sign of dE_{dir}/dT as the bands invert [14]. Interestingly, for composition $Pb_{0.44}Sn_{0.56}Te$, in which a temperature dependent inversion takes place, a minimum in E_{dir} is observed at the inversion temperature, in contrast to a plateauing value for E_{dir} in our data. Since our $\omega_p^2(T)$ and $\epsilon_\infty(T)$ data suggest that the direct gap E_g is zero at 160 ± 15 K, Eq. (4) predicts that our observed plateauing E_{dir}
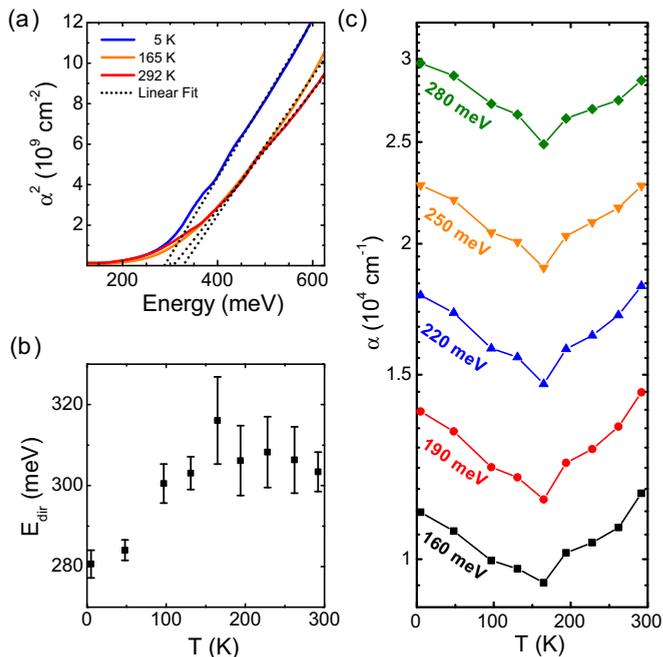
FIG. 3. (Color online) (a) Linear fits of the squared absorption coefficient yield the smallest observable direct band transition energy (x intercept). (b) Direct gap transition extracted from the linear fit. (c) Absorption coefficient (logarithmic scale) below E_{dir}, revealing a distinct change in temperature dependence, uncharacteristic for an Urbach tail.

is either due to a change in μ, or a change in m_c/m_v across the transition. While previous theory work [28] shows that both μ and m_c change as E_g changes, further theoretical investigations are required to be certain of the relative contributions of $\mu(T)$ vs the conduction-valence band (a)symmetry [i.e. $m_c/m_v(T)$].

We find a minimum direct transition of 280 meV at 5 K, which is larger than the low temperature direct transition of 200–250 meV shown by previous ARPES results [25,27,29,30,51]. This difference is expected considering our larger carrier density compared to previous reports, as we show later in Sec. III E ("DC Transport"). We also note that the sensitivity to surface states in ARPES conceals bulk signatures, complicating the estimation of bulk transition energies.

We now consider the spectral weight below the direct transition energy E_{dir}. This is often explained as an Urbach tail, which results from disorder in the crystal, and has an exponential energy dependence that changes monotonically with temperature [11,47]. While Fig. 3(a) does show exponential behavior below E_{dir} ($\sim$280 meV), a closer look at $\alpha(T)$ at various frequencies in Fig. 3(c) reveals atypical Urbach behavior. Instead of a monotonic temperature dependent change of the exponential behavior, a distinct minimum is observed at 160 K, while at both lower and higher temperatures the spectral weight in the absorption coefficient increases. Although it is not surprising that transitions below the direct gap are sensitive to the band inversion, the exact details of their temperature dependence are not clear and require future theory and experiment. Nonetheless, this shows that the absorption and optical conductivity are useful tools in studying a band inversion.

D. Extended Drude analysis and scattering rate

To study the bulk carrier lifetime in $\text{Pb}_{0.77}\text{Sn}_{0.23}\text{Se}$, we now turn to the extended Drude model. From Eq. (1), it can be seen that the free carrier response in the standard Drude model is fully defined by ϵ_∞, ω_p, and τ, where τ is the static transport lifetime resulting from a sum of all scattering processes according to Matthiessen's rule (including impurity, electron-phonon, and electron-electron scattering) [55]. While the Drude model is frequently used to study scattering mechanisms that can be distinguished by their temperature dependence, the temperature dependent band inversion in $\text{Pb}_{0.77}\text{Sn}_{0.23}\text{Se}$ severely complicates such analysis. Moreover, the standard Drude model does not consider the energy dependence of the lifetime $\tau(\omega)$. Since the carrier lifetime is an important parameter for thermoelectric efficiency [56] we turn to the extended Drude model, in which the lifetime has an energy dependence given by [18]

$$\frac{1}{\tau(\omega)} = -\frac{\omega_p^2}{\omega}\,\text{Im}\left(\frac{1}{\hat{\epsilon}(\omega) - \epsilon_\infty}\right). \tag{5}$$

Figure 4 shows the frequency dependent scattering rate obtained using Eq. (5). To study the nature of the dominant scattering mechanism, the data were fitted [red dotted lines in Fig. 4(a)] using the empirical relation

$$\frac{1}{\tau(\omega)} = \frac{1}{\tau_{\text{DC}}} + \beta\omega^n, \tag{6}$$

where $1/\tau_{\text{DC}} = \alpha T^m + 1/\tau_{\text{imp}}$. Here, $1/\tau_{\text{imp}}$ accounts for impurity scattering, and α and β are constants that depend on material properties. When $n = m = 2$, and for certain values of α/β, Eq. (6) resembles the single-particle scattering rate within Fermi-liquid theory, in which electron-electron scattering dominates the transport properties [20].

Figure 4(b) shows $1/\tau_{\text{DC}}$, obtained from the fits with Eq. (6). As the temperature is raised, $T^{3/2}$ behavior is observed (dashed red line), associated with electron-acoustic phonon scattering in semiconductors [54,55]. This is consistent with most good thermoelectrics, in which electron-acoustic phonon scattering dominates the transport properties [7,57–59]. Perhaps somewhat unexpected, however, is that the band inversion appears to have no bearing on $1/\tau_{\text{DC}}$. This is contrasted by recent work by Wu *et al.* [40], in which the scattering rate of carriers in $(\text{Bi}_{1-x}\text{In}_x)_2\text{Se}_3$ was found to diverge going across the topological phase transition as a function of doping.

We note that unlike the $(\text{Bi}_{1-x}\text{In}_x)_2\text{Se}_3$ study, where μ was located in the bottom of the conduction band, we are much more sensitive to bulk carriers (as μ is high in the conduction band). Hence, we do not expect to see such a divergence, but it is worth emphasizing that more resistive $\text{Pb}_{1-x}\text{Sn}_x\text{Se}$ samples (in which the surface contributions are enhanced) may exhibit similar behavior. For such samples, the frequency dependent scattering rate may also serve as a novel analytical technique to discriminate surface states from the bulk. Since surface states are protected from backscattering, their lifetimes are expected to exceed the bulk carrier lifetime. This could result in distinct surface and bulk scattering contributions in $1/\tau(\omega)$, for which we see no evidence in our samples. From fitting $1/\tau_{\text{DC}}$, we also find a constant $1/\tau_{\text{imp}} = 6.8 \pm 0.3$ meV, attributed to impurity scattering. We note that in metals and
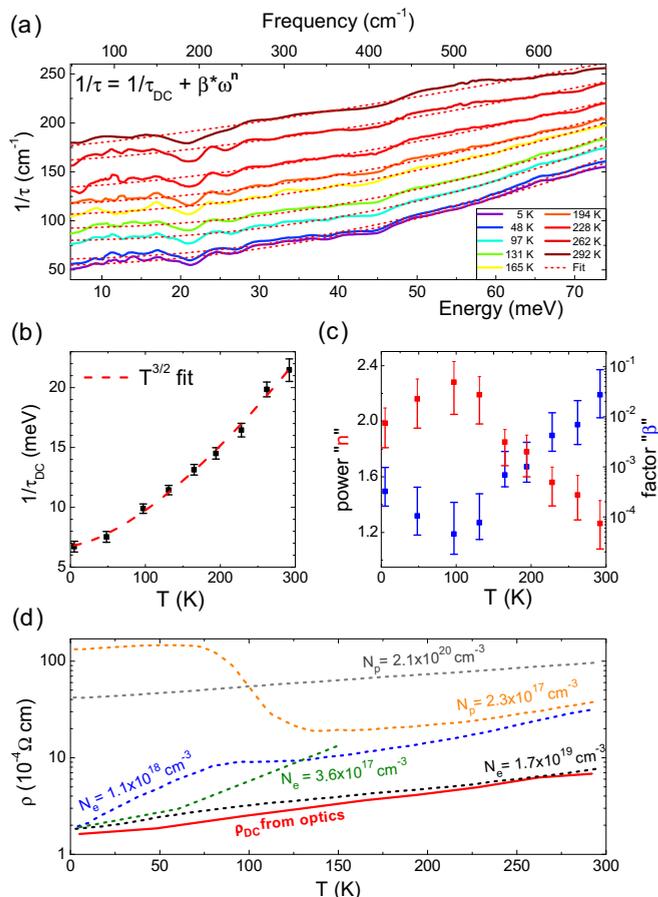
FIG. 4. (Color online) (a) Power-law fits of the frequency dependent scattering rate. (b) A $T^{3/2}$ fit (red dashed line) of the temperate dependent static scattering rate $1/\tau_{DC}$ illustrates phonon dominated scattering. (c) Fitting parameters n and β. (d) Comparison of Pb$_{0.77}$Sn$_{0.23}$Se resistivity obtained by optical spectroscopy (solid red line), and by standard DC transport methods by Liang *et al.* [6] (green dotted line), and Dixon *et al.* [8] (all other data).

degenerate semiconductors such as as-grown Pb$_{0.77}$Sn$_{0.23}$Se, the electronic impurity scattering rate $1/\tau_{imp}^{\sigma}$ is roughly equal to the thermal impurity scattering lifetime $1/\tau_{imp}^{\kappa}$ [55].

Figure 4(c) shows the temperature dependence of fitting parameters n and β. Since we were only able to obtain reliable $1/\tau(\omega)$ data over a limited range spanning just one decade in energy [as seen in Fig. 4(a)], we hesitate to attribute any physical meaning to either parameter. Additional measurements at lower frequencies and temperatures, or detailed studies by alternative probes such as high resolution, temperature dependent ARPES could offer greater insights, but are beyond the scope of this work. Nevertheless, with $n = 2$ normally associated with Fermi liquid type electron-electron dominated scattering at low temperatures [20], the observed values of $n \sim 2$ up to 160 K is quite surprising, making it an interesting starting point for followup studies.

E. DC transport

For comparison with previous transport studies of Pb$_{0.77}$Sn$_{0.23}$Se, we calculate its DC conductivity using $\sigma_o =$

$\omega_p^2 \tau_{DC}/60$ and find $\sigma_o = 6.2 \times 10^3$ Ω^{-1}cm^{-1} at 5 K. This low temperature value is in good agreement with previous transport results of *n*-type samples with identical stoichiometry (6.7 $\times$ 10^3 Ω^{-1}cm^{-1} by Dixon *et al.* [8] and 5.5 $\times 10^3$ Ω^{-1}cm^{-1} by Liang *et al.* [6]). A comparison of the resistivity with previously published data is shown in Fig. 4(d), where the dashed lines are digitized data from Liang *et al.* [6] (green) and Dixon *et al.* [8] (all other colors). We note that all *n*-type crystals increase in resistance with temperature, typical for metals and degenerate semiconductors. Only the resistivity of a low carrier *p*-type sample measured by Dixon *et al.* [8] shows an anomaly between 75 and 200 K, possibly associated with the band inversion temperature, while none of the *n*-type curves reveal such signatures. This further illustrates the utility of optical spectroscopy, which can simultaneously determine ω_p and $1/\tau$ to find σ_0, while also measuring E_F (via direct transitions) and the inversion temperature.

A possible explanation for the difference between *n*-type and *p*-type resistivity behavior is the asymmetry of the conduction and valance band, which can be tested by comparing their respective band masses. Using the carrier density of $N_e = 1.7 \times 10^{19}$ cm^{-3} (from the resistivity curve most similar to our our results), we find a mobility of 2260 cm^{2}V^{-1}s^{-1}, and a band mass of $m_b = 0.076 m_e$, using $\sigma_o = 4\pi n e^2 \tau(\omega)/m_b$. This band mass is smaller than the value of $0.1 m_e$ found by Dixon *et al.* for *p*-type Pb$_{0.77}$Sn$_{0.23}$Se, thus confirming the asymmetry between conduction and valence band. Using Eq. (4) we can now estimate the value of μ ($\approx E_F$), using the low temperature direct gap value of $E_g = 80 \pm 20$ meV, consistent with previous studies and calculations [9,29,30]. We find a value for μ of 114 ± 22 meV. To further corroborate this value, we derive an expression for E_F using the parabolic band approximation. Starting with $E_F = \hbar^2 k_F^2/2m_b$, and substituting the three-dimensional (3D) carrier density $n_{3D} = \frac{1}{(2\pi)^3}\frac{4}{3}\pi k_F^3 g_s g_v$, we get

$$E_F = \frac{\hbar^2}{2m_b}\left(\frac{6\pi^2 n}{g_s g_v}\right)^{2/3}, \tag{7}$$

where $g_s = 2$ and $g_v = 4$ are the bulk spin and valley degeneracy, respectively [6,29]. Substituting the plasma frequency in SI units into Eq. (7), where $\omega_p^2 = ne^2/m_b\epsilon_0$, we find an expression for E_F in eV as a function of physical constants, ω_p^2 in rad/s and n in m^{-3}:

$$E_F = \frac{\hbar^2 \omega_p^2 \epsilon_0}{2e^3 n^{1/3}}\left(\frac{6\pi^2}{g_s g_v}\right)^{2/3}. \tag{8}$$

Equation (8) yields a value for E_F ($\approx \mu$) of 126 meV at 5 K, which is consistent with our value of μ of 114 ± 22 meV obtained from the direct gap transitions (see Sec. III C), and further confirms the metallic character of naturally doped *n*-type Pb$_{0.77}$Sn$_{0.23}$Se. As explained in Sec. III B, this further confirms why surface states are not observed in the reflectance spectra.

F. Power factor

Finally, we relate our obtained values for σ_o and μ to the Seebeck coefficient $S(T)$ and the power factor $S^2\sigma_o(T)$. In the parabolic band approximation, the Seebeck coefficient is given
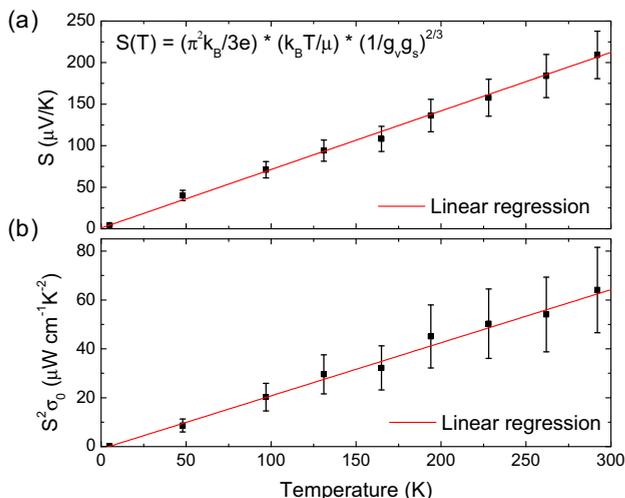
FIG. 5. (Color online) (a) A linear regression of the Seebeck coefficient in the parabolic band assumption, where all changes in E_{dir} are attributed to changes in E_F. (b) The power factor indicates minimal (if any) sensitivity to the suggested band inversion at 160 ± 15 K, as a result of the high chemical potential.

by [3] $S = \frac{8\pi^2 k_B^2}{3eh^2} m_b T (\frac{\pi}{3n})^{2/3}$ (where m_b is the conduction of valance band mass), which can be expressed as a function of E_F [using Eq. (7)] as

$$S(T) = \left(\frac{\pi^2 k_B}{3e}\right)\left(\frac{k_B T}{E_F}\right)\left(\frac{1}{g_s g_v}\right)^{2/3}. \qquad (9)$$

Since μ is located high in the conduction band, the direct gap transitions are likely only minimally sensitive to changes in the true band gap E_g (and thus m_c) as a function of temperature. This is illustrated in the left and right panels in Fig. 2(a), showing a similar band dispersion for high μ despite a dramatic change in the band gap. Hence, we can estimate the maximum change in $S(T)$ by attributing the temperature dependence of $E_{\mathrm{dir}}(T)$ [see Eq. (4)] entirely to changes in $\mu(T)$. The result of this estimation, after substituting $\mu(T)$ for E_F in Eq. (9), is plotted in Fig. 5(a), while Fig. 5(b) shows the associated power factor $S^2 \sigma_0$. It is clear that neither S nor $S^2 \sigma_0$ show distinct signatures of a band inversion, while both increase linearly with temperature. These results suggests that there is room for optimization of the figure of merit ZT in Pb$_{1-x}$Sn$_x$Se compounds where μ is located deep in the conduction band. Further doping to alter the lattice and suppress phonon contributions will likely only affect the electronic response minimally, as illustrated by its insensitivity to the band inversion and the unaffected power factor.

IV. DISCUSSION

It is clear from our data that, for application of Pb$_{0.77}$Sn$_{0.23}$Se as either a topological crystalline insulator or thermoelectric, the high electrical conductivity of bulk states is a major prohibitive factor. Moreover, some of the fundamental physics governing the electronic, thermal, and topological properties are difficult to probe due to the high chemical potential in as-grown Pb$_{0.77}$Sn$_{0.23}$Se. Hence, future studies on samples in the Pb$_{1-x}$Sn$_x$Se series, in which the carrier

density has been reduced, could lead to new insights into the interplay of phonons, thermal and electronic bulk lifetimes, and the optical and electronic properties of inversion symmetry protected topological surface states.

A reduction of the chemical potential would also enhance the sensitivity of the Seebeck coefficient to the band inversion, which could potentially result in a dramatic enhancement of the figure of merit ZT around the band inversion. Moreover, alternative stoichiometries also offer an interesting avenue, as previous measurements suggest that the band inversion in Pb$_{1-x}$Sn$_x$Se could be pushed to higher temperatures—relevant to many thermoelectric applications—by increasing the Sn content [8,9,29]. Hence, by optimizing Se doping, an ideal Pb$_{1-x}$Sn$_x$Se stoichiometry can be determined, in which ZT peaks around a desired temperature range. Indeed, such doping studies would also allow for the study of the high temperature interplay between the topologically nontrivial phase and thermoelectric efficiency, which is a direction currently unexplored.

V. CONCLUSION

In conclusion, we have performed broadband optical spectroscopy experiments on as-grown n-type Pb$_{0.77}$Sn$_{0.23}$Se and extracted its optical constants over a temperature range between 5 and 293 K. By studying the plasma frequency and band gap transitions, we find clear signatures suggestive of the temperature dependent band inversion at 160 ± 15 K, despite the chemical potential being far in the conduction band. We note that since temperature is an easily controllable variable in optical spectroscopy, in principle this could be used to optically determine band inversion temperatures of conductive samples with extremely high precision. While the band inversion of Pb$_{0.77}$Sn$_{0.23}$Se is also associated with a topological phase transition [6,29–31,33,51,53], we do not see any signatures of surface states, and thus do not comment on the topology of the band structure on either side of the band inversion. This is an expected result, however, as optical modeling suggests that the highly conductive bulk carriers dominate the properties of as-grown Pb$_{0.77}$Sn$_{0.23}$Se.

By performing extended Drude analysis, we accurately determine the temperature dependent scattering rate, and find that it follows $T^{3/2}$ behavior (associated with electron-acoustic phonon interactions) typical for good thermoelectrics [57], superimposed on a constant impurity scattering background with $1/\tau = 6.8 \pm 0.3$ meV. The frequency dependence of the scattering rate shows no evidence of different scattering channels below and above the suggested band inversion temperature, but data over a greater energy and temperature range are required for more conclusive results. Moreover, neither the DC resistivity, Seebeck coefficient, or the power factor show any evidence of the band inversion. These results confirm earlier transport studies on similar compounds [9–12,23,24,32], and emphasizes the utility of optical spectroscopy in the study of thermoelectrics and/or band inversions.

With both thermoelectrics and topological (crystalline) insulators offering numerous appealing applications in industry, while presenting nontrivial physical characterization and optimization challenges, a better understanding of fundamental physics governing the figure of merit ZT and the isolation

of surface conductance are of both practical and fundamental interest. The Pb$_{1-x}$Sn$_x$Se and Pb$_{1-x}$Sn$_x$Te series offer many exciting opportunities in this pursuit, particularly through optical investigations, by combining several novel physical phenomena into a single temperature tunable system.

APPENDIX: EXPECTED OPTICAL SIGNATURES OF TCI SURFACE STATES IN Pb$_{0.77}$Sn$_{0.23}$Se

To ensure we did not overlook surface state signatures in our reflectance data, we use the Boltzmann transport equation to estimate the expected effect of surface states on the measured reflectance. The 2D surface state plasma frequency can be approximated by $\omega_{p,2D}^2 = (e^2/h)2\pi k_F v_F g_s g_v$, where v_F and k_F are the Fermi velocity and wave vector, and g_s and g_v are the spin and valley degeneracies [35,39,60]. Ignoring the parabolic correction for the Dirac states, we can use $E_F = \hbar k_F v_F$, and express $(\hbar\omega_{p,2D})^2$ in a convenient form with all SI units:

$$(\hbar\omega_{p,2D})^2 = c^2 e E_F g_s g_v 10^{-5} \tag{A1}$$

where c is the speed of light and e is the elementary charge. From previous ARPES measurements, we can estimate a surface Fermi level E_F^{ss} around 125 meV [29]. At the risk of overestimating the surface contribution, we can account for sample-to-sample variations by considering an even higher surface state Fermi level of 200 meV. We also note that while $g_s = 1$ and $g_v = 2$ near the Dirac point, additional Dirac states with smaller wave vectors intersect the Fermi surface when the
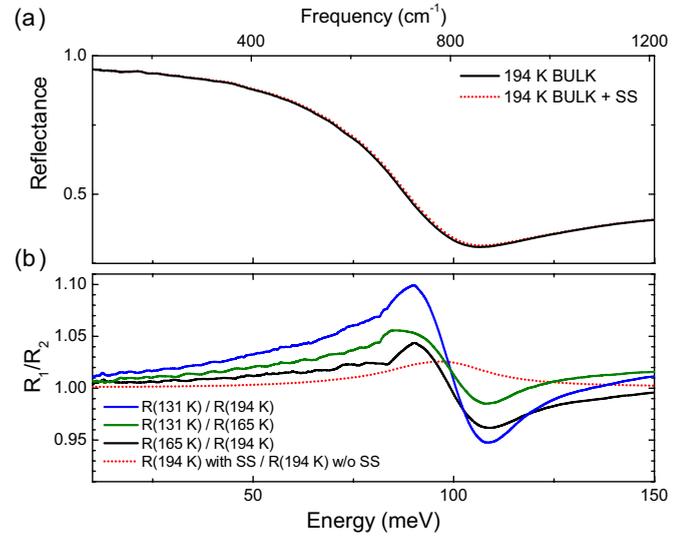
FIG. 6. (Color online) (a) Reflectance of Pb$_{0.77}$Sn$_{0.23}$Se at 194 K, and a model of the 194 K reflectance that included a surface state layer with $\omega_{p,2D} = 0.34$ meV cm$^{1/2}$. (b) Ratios of the temperature dependent reflectance above (black), below (green), and across (blue) the topological phase transition. The dotted red line is the ratio of reflectance spectra from (a), illustrating the much larger effect of temperature on $R(\omega)$ compared to the introduction of surface states below the topological phase transition.

Fermi level crosses the bulk conduction band, thus doubling the surface bands, albeit with different wave vectors [6,29,53,61]. For convenience, we account for these states by setting $g_v = 4$, resulting in a overestimated 2D plasma frequency of 0.12 meV^{2}cm.

Figure 6(a) shows the reflectance of Pb$_{0.77}$Sn$_{0.23}$Se at 192 K (the topologically trivial regime) as well as a model in which a surface state layer with $\hbar\omega_{p,2D} = 0.34$ meV cm$^{1/2}$ was added to the 192 K reflectance. To emphasize the minimal difference, Fig. 6(b) shows the ratio of both reflectance spectra (red dotted line). The same plot also shows the ratio of reflectance measurements at different temperatures above (black), below (green), and across (blue) the topological phase transition. It is clear that the sharpening bulk plasma edge has a far greater effect on the reflectance, than the surface states. Hence, discriminating surface state signatures are not within our measurement capabilities for samples with such high bulk carrier densities.

[1] M. Zebarjadi, K. Esfarjani, M. S. Dresselhaus, Z. F. Ren, and G. Chen, Energy Env. Sci. **5**, 5147 (2012).

[2] S. B. Riffat and X. Ma, Appl. Thermal Eng. **23**, 913 (2003).

[3] G. J. Snyder and E. S. Toberer, Nat. Mater. **7**, 105 (2008).

[4] F. J. Di Salvo, Science **285**, 703 (1999).

[5] J. P. Heremans Font, Acta Phys. Pol. A **108**, 609 (2005).

[6] T. Liang, Q. Gibson, J. Xiong, M. Hirschberger, S. P. Koduvayur, R. J. Cava, and N. P. Ong, Nat. Commun. **4**, 2696 (2013).

[7] O. Delaire, J. Ma, K. Marty, A. F. May, M. A. McGuire, M.-H. Du, D. J. Singh, A. Podlesnyak, G. Ehlers, M. D. Lumsden, and B. C. Sales, Nat. Mater. **10**, 614 (2011).

[8] J. R. Dixon and G. F. Hoff, Phys. Rev. B **3**, 4299 (1971).

[9] A. J. Strauss, Phys. Rev. **157**, 608 (1967).

[10] M. Baleva, T. Georgiev, and G. Lashkarev, J. Phys. Condens. Matter **2**, 2935 (1990).

[11] Z. M. Gibbs, A. LaLonde, and G. J. Snyder, New J. Phys. **15**, 075020 (2013).

[12] C. E. Ekuma, D. J. Singh, J. Moreno, and M. Jarrell, Phys. Rev. B **85**, 085205 (2012).

[13] J. Zhao, C. D. Malliakas, D. Bugaris, N. Appathurai, V. Karlapati, D. Y. Chung, M. G. Kanatzidis, and U. Chatterjee, arXiv:1404.1807.

[14] S. O. Ferreira, E. Abramof, P. Motisuke, P. H. O. Rappl, H. Closs, A. Y. Ueta, C. Boschetti, and I. N. Bandeira, Braz. J. Phys. **29**, 771 (1999).

[15] Z. M. Gibbs, H. Kim, H. Wang, R. L. White, F. Drymiotis, M. Kaviany, and G. Jeffrey Snyder, Appl. Phys. Lett. **103**, 262109 (2013).

[16] J. Allen and J. Mikkelsen, Phys. Rev. B **15**, 2952 (1977).

[17] D. N. Basov and T. Timusk, Rev. Mod. Phys. **77**, 721 (2005).

[18] M. M. Qazilbash, J. J. Hamlin, R. E. Baumbach, L. Zhang, D. J. Singh, M. B. Maple, and D. N. Basov, Nat. Phys. **5**, 647 (2009).

[19] D. Basov, R. Averitt, D. van der Marel, M. Dressel, and K. Haule, Rev. Mod. Phys. **83**, 471 (2011).

[20] U. Nagel, T. Uleksin, T. Room, R. P. S. M. Lobo, P. Lejay, C. C. Homes, J. S. Hall, A. W. Kinross, S. K. Purdy, T. Munsie, T. J. Williams, G. M. Luke, and T. Timusk, Proc. Natl. Acad. Sci. **109**, 19161 (2012).

[21] J. Hwang, T. Timusk, and G. D. Gu, J. Phys. Condens. Matter **19**, 125208 (2007).

[22] S. I. Mirzaei, D. Stricker, J. N. Hancock, C. Berthod, A. Georges, E. Van Heumen, M. K. Chan, X. Zhao, Y. Li, M. Greven, and D. van der Marel, Proc. Natl. Acad. Sci. **110**, 5774 (2013).

[23] R. K. Shukla, S. K. Shukla, V. K. Pandey, and P. Awasthi, Phys. Chem. Liq. **45**, 169 (2007).

[24] L.-D. Zhao, S.-H. Lo, Y. Zhang, H. Sun, G. Tan, C. Uher, C. Wolverton, V. P. Dravid, and M. G. Kanatzidis, Nature (London) **508**, 373 (2014).

[25] B. M. Wojek, P. Dziawa, B. J. Kowalski, A. Szczerbakow, A. M. Black-Schaffer, M. H. Berntsen, T. Balasubramanian, T. Story, and O. Tjernberg, Phys. Rev. B **90**, 161202 (2014).

[26] N. Anand, S. Buvaev, A. F. Hebard, D. B. Tanner, Z. Chen, Z. Li, K. Choudhary, A. B. Sinnott, G. Gu, and C. Martin, preceding paper, Phys. Rev. B **90**, 235143 (2014).

[27] M. Neupane, S.-Y. Xu, R. Sankar, Q. Gibson, Y. J. Wang, N. Alidoust, G. Bian, C. Liu, I. Belopolski, Y. Ohtsubo, A. Taleb-Ibrahimi, S. Basak, W. F. Tsai, H. Lin, R. J. Cava, A. Bansil, F. C. Chou, and M. Z. Hasan, arXiv:1403.1560.

[28] G. Martinez, Phys. Rev. B **8**, 4678 (1973).

[29] P. Dziawa, B. J. Kowalski, K. Dybko, R. Buczko, A. Szczerbakow, M. Szot, E. Łusakowska, T. Balasubramanian, B. M. Wojek, M. H. Berntsen, O. Tjernberg, and T. Story, Nat. Mater. **11**, 1023 (2012).

[30] B. M. Wojek, R. Buczko, S. Safaei, P. Dziawa, B. J. Kowalski, M. H. Berntsen, T. Balasubramanian, M. Leandersson, A. Szczerbakow, P. Kacman, T. Story, and O. Tjernberg, Phys. Rev. B **87**, 115106 (2013).

[31] X. Xi, X.-G. He, F. Guan, Z. Liu, R. D. Zhong, J. A. Schneeloch, T. S. Liu, G. D. Gu, D. Xu, Z. Chen, X. G. Hong, W. Ku, and G. L. Carr, Phys. Rev. Lett. **113**, 096401 (2014).

[32] J. F. Butler, A. R. Calawa, and T. C. Harman, Appl. Phys. Lett. **9**, 427 (1966).

[33] L. Fu, Phys. Rev. Lett. **106**, 106802 (2011).

[34] S.-Y. Xu, C. Liu, N. Alidoust, M. Neupane, D. Qian, I. Belopolski, J. D. Denlinger, Y. J. Wang, H. Lin, and L. A. Wray, Nat. Commun. **3**, 1192 (2012).

[35] A. A. Reijnders, Y. Tian, L. J. Sandilands, G. Pohl, I. D. Kivlichan, S. Y. Frank Zhao, S. Jia, M. E. Charles, R. J. Cava, N. Alidoust, S. Xu, M. Neupane, M. Z. Hasan, X. Wang, S. W. Cheong, and K. S. Burch, Phys. Rev. B **89**, 075138 (2014).

[36] R. Valdés Aguilar, A. V. Stier, W. Liu, L. S. Bilbro, D. K. George, N. Bansal, L. Wu, J. Černe, A. G. Markelz, S. Oh, and N. P. Armitage, Phys. Rev. Lett. **108**, 087403 (2012).

[37] G. S. Jenkins, D. C. Schmadel, A. B. Sushkov, and H. D. Drew, Phys. Rev. B **87**, 155126 (2013).

[38] P. Di Pietro, M. Ortolani, O. Limaj, A. Di Gaspare, V. Giliberti, F. Giorgianni, M. Brahlek, N. Bansal, N. Koirala, S. Oh, P. Calvani, and S. Lupi, Nature (London) **8**, 556 (2013).

[39] B. C. Chapler and D. N. Basov (private communication).

[40] L. Wu, M. Brahlek, R. V. Aguilar, A. V. Stier, C. M. Morris, Y. Lubashevsky, L. S. Bilbro, N. Bansal, S. Oh, and N. P. Armitage, Nat. Phys. **9**, 410 (2013).

[41] Z. Li and J. P. Carbotte, Phys. Rev. B **88**, 045414 (2013).

[42] X. Xi, C. Ma, Z. Liu, Z. Chen, W. Ku, H. Berger, C. Martin, D. B. Tanner, and G. L. Carr, Phys. Rev. Lett. **111**, 155701 (2013).

[43] M. K. Tran, J. Levallois, P. Lerch, J. Teyssier, A. B. Kuzmenko, G. Autès, O. V. Yazyev, A. Ubaldini, E. Giannini, D. van der Marel, and A. Akrap, Phys. Rev. Lett. **112**, 047402 (2014).

[44] P. Di Pietro, F. M. Vitucci, D. Nicoletti, L. Baldassarre, P. Calvani, R. Cava, Y. S. Hor, U. Schade, and S. Lupi, Phys. Rev. B **86**, 045439 (2012).

[45] A. D. La Forge, A. Frenzel, B. C. Pursley, T. Lin, X. Liu, J. Shi, and D. N. Basov, Phys. Rev. B **81**, 125120 (2010).

[46] A. Akrap, M. Tran, A. Ubaldini, J. Teyssier, E. Giannini, D. van der Marel, P. Lerch, and C. C. Homes, Phys. Rev. B **86**, 235207 (2012).

[47] C. H. Grein and S. John, Phys. Rev. B **39**, 1140 (1989).

[48] L. Benfatto, S. G. Sharapov, N. Andrenacci, and H. Beck, Phys. Rev. B **71**, 104511 (2005).

[49] F. Carbone, A. B. Kuzmenko, H. J. A. Molegraaf, E. van Heumen, E. Giannini, and D. van der Marel, Phys. Rev. B **74**, 024502 (2006).

[50] M. Ortolani, P. Calvani, and S. Lupi, Phys. Rev. Lett. **94**, 067002 (2005).

[51] A. Gyenis, I. K. Drozdov, S. Nadj-Perge, O. B. Jeong, J. Seo, I. Pletikosic, T. Valla, G. D. Gu, and A. Yazdani, Phys. Rev. B **88**, 125414 (2013).

[52] A. B. Kuzmenko, D. van der Marel, F. Carbone, and F. Marsiglio, New J. Phys. **9**, 229 (2007).

[53] Y. Okada, M. Serbyn, H. Lin, D. Walkup, W. Zhou, C. Dhital, M. Neupane, S. Xu, Y. J. Wang, R. Sankar, F. Chou, A. Bansil, M. Z. Hasan, S. D. Wilson, L. Fu, and V. Madhavan, Science **341**, 1496 (2013).

[54] P. Y. Yu and M. Cardona, *Fundamentals of Semiconductors*, 4th ed. (Springer, Berlin 2010).

[55] J. Singleton, *Band Theory and Electronic Properties of Solids* (Oxford University Press, Oxford, 2010).

[56] M. Jonson and G. D. Mahan, Phys. Rev. B **21**, 4223 (1980).

[57] Y. Pei, X. Shi, A. LaLonde, H. Wang, L. Chen, and G. J. Snyder, Nature (London) **473**, 66 (2011).

[58] H. Wang, Y. Pei, A. D. LaLonde, and G. J. Snyder, Adv. Mater. **23**, 1366 (2011).

[59] Y. I. Ravich, B. A. Efimova, and V. I. Tamarchenko, Phys. Status Solidi B **43**, 11 (1971).

[60] S. Adam, E. H. Hwang, V. M. Galitski, and S. Das Sarma, Proc. Natl. Acad. Sci. **104**, 18392 (2007).

[61] J. Liu, W. Duan, and L. Fu, Phys. Rev. B **88**, 241303 (2013).